united nations
educational, scientific
and cultural
organization

international atomic
energy agency

the
abdus salam
international centre for theoretical physics

SMR 1273 - 5

WORKSHOP ON PLASMA DIAGNOSTICS AND INDUSTRIAL APPLICATIONS OF PLASMAS

12 - 13 OCTOBER 2000

INDUSTRIAL APPLICATIONS OF SMALL PLASMA DEVISES AND RELATED DIAGNOSTICS

Jorge FEUGEAS
Rosario Institute of Physics (IFIR)
Bv. 27 de Febrero 210 Bis.
2000 Rosario, Argentina

INDUSTRIAL APPLICATIONS OF SMALL PLASMA DEVISES AND RELATED DIAGNOSTICS**

Jorge Feugeas*

Rosario Institute of Physics (IFIR), Bv. 27 de Febrero 210 Bis. 2000 Rosario, Argentina

(*) **Researcher of CONICET, and Professor of the University of Rosario, Argentina**

(**) **Research supported by the following institutions: International Atomic Energy Agency, Viena, Austria; National Council of Research, Argentina; Agencia para la Promoción de la Investigación Científica y Tecnológica, Argentina; University of Rosario, Argentina; Antorchas Foundation, Argentina; Vitae Foundation, Brazil; TWAC, ICTP, Trieste, Italy.**

[The Laboratory is part of PIPAD (Interinstitutional Program on Dense Plasmas), Argentina]

1- INTRODUCTION

Plasma physics is a discipline that has suffered enormous evolutions over the last decades. The effort done in the field of nuclear fusion for example, gives an impulse not only to the basic research (theoretical and experimental) in plasma physics, but also to the development of techniques in plasma production and diagnostic techniques. Also microelectronics, that evolved rapidly allowing rapid progress in many fields such as computer science, had the benefits of the evolution of plasma physics. In most of the semiconductor technology, plasmas are directly or indirectly involved: surface treatment, doping, architecture of the highly integrated circuits, etc.

The advances in plasma physics give many other benefits such as those observed in astrophysics (a better comprehension of the earth's magnetosphere, the interplanetary and intergalactic space, etc). Also in this field, the technology derived from plasma physics in laboratories, allowed the development of accurate instrumental for plasma testing in space.

Considering all the mentioned fields of applications (nuclear fusion, microelectronics, space exploration, etc.) the conclusion could be that the economic effort necessary to carry out applied projects makes it difficult in developing countries to work on technology in which plasma physics is involved. The prime idea could be that in the developing countries only working in basic research should be possible, to succeed with some novel results. Nevertheless, there are many other fields that can be engaged succesfully in the applied field including, with enormous possibilities of industrial transferal. In this last aspect, it is necessary to take into account the existence of real possibilities of producing goods through the technology based on plasma physics. Those technologies can be based on relative low cost processes, leading to well positioned technologies in the world market.

In this work I will present our experience in plasma physics applied research, and some concrete demands in Argentina.

Since 1986 the Plasma Physics Group of IFIR is working in experiments related to the application of plasmas to the surface treatment of metals and alloys. In the first stage, the research was concentrated in the use of high energy and short duration pulse plasmas, process known as *thermal shock*. More recently, in 1992, the research was extended to the use of *cold plasmas* in processes with the similar purpose of surface treatment.

2- HIGH ENERGY PULSE PLASMAS

The process consists in the irradiation of surfaces with high energy and short duration pulses of plasmas, inducing in the surfaces a rapid thermal evolution plus the atom implantation when active species like nitrogen are used. In our experiments, the plasma emmision from a Mather type Plasma Focus (Z-pinch experiment) was used. This process can be assimilated to a fast ion implantation process.

Ion implantation is a well-known technique for the surface treatment of metals for tribological property improvements, among other applications [1]. A large variety of ion species, energies and fluences can be used depending on the substrate nature and the final surface properties desired [2-3].

In this work, we describe the results of steel, pure titanium, copper, and other metals and alloys nitrogen implanted with ion beams belonging to pulsed plasmas accelerated in focalized electric discharges in a coaxial electrode system operated in the detonation mode (Plasma Focus) [4]. These ion beams present several differences with respect to the standard one of low current and continuous ion beams, principally due to the short duration of the pulses, which provokes strong thermal effects on the surface layers, in addition to the proper on implantation process.

We also present the results of the characterization of the process that allow, to some extent, the explanation of the physics in this pulsed ion implantation process.

Plasma Focus (PF) is an experiment in which a fast and energetic electric discharge is produced in a low pressure atmosphere, between two coaxial electrodes. As a consequence, at the open end of the coaxial electrode system, a column of dense plasma or Dense Plasma Focus (DPF) is formed, reaching high density and high (thermonuclear) temperatures, with a high efficiency in nuclear fusion reactions [4,5].

Nevertheless, and due to the energetic processes involved, other physical phenomena take

place which allow interesting applications. One of them is the ion and electron beam acceleration. During the DPF formation, Rayleigh Taylor instabilities take place giving rise to strong electric fields that can accelerate ions and electrons to high energies. These particle beams have been object of study not only under the scientific point of view, but also because of its potential use in industrial applications. One of the recent studies had been connected to the use of ion beams in surface treatment of materials for tribological improvement purposes. As a Pulsed Ion Beam Implanter for example, Feugeas et al [6] showed the satisfactory performance of this device in metal (steel, titanium, etc.) surface hardening and in friction and wear reduction.

2.1- Mather type Plasma Focus: experiment description

The device used in the experiments was a Mather type Plasma Focus that is essentially a Z-pinch. Our PF [6] consisted of a coaxial electrode system open at one end and closed, but separated by an also coaxial insulator, at the other (see Figure 1). The electrodes were allocated in a discharge chamber, which was filled with a pure gas at a controlled pressure. The anode (center electrode) was a cylinder built in brass with an effective length of 72 mm and an external diameter of 17.5 mm, with a wall thickness of 2 mm. The external electrode had an effective length of 70 mm with an internal diameter of 50 mm, and the insulator (Pyrex pipe) had an effective length of 27 mm with an external diameter of 24.5 mm.

The electrodes were connected to a capacitor bank through a transmission line and the discharge was controlled by a fast switch (spark-gap). The total capacity of our capacitor bank was 3.8 μf and in the experiments it was charged to a voltage of 20 kV giving storage energy of 0.76 kJ.

For a well designed system, when the capacitor bank is discharged into the electrodes, the break down (BD) is produced as a gliding current sheath built up on the insulator surface (cylindrical plasma sheath). This plasma sheath, through which the discharged current circulates, begins to move (run-down stage, RD) through the inter-electrode space to the open coaxial gun end accelerated by the magnetic pressure (Lorentz force originated by the interaction between the current and the self-generated magnetic field). At the end of the electrodes, the plasma sheath begins to roll-off (RO) converging into the symmetry axis of the system, developing a dense plasma column or dense plasma focus (DPF) in front of the anode. This DPF column, in PF with the characteristics of our system, has a length of ~10 mm and a diameter < 1 mm as observed in images taken with Image Converter Cameras [7]. For an optimized design of the system this compression has to occur approximately at a time $\tau/4$ (τ being the period of the oscillating

component of the discharge), time in which the electric current **I(t)** reaches the maximum value I_M. Our system had a τ = 3.4 μs, and $I_M \sim$ 200 kA. If this occurs, in the DPF column a pinch instability takes place, giving rise to several energetic processes like acceleration of electron and ion beams, bursts of x-rays, microwaves and radiation in other regions of the electromagnetic spectrum, neutron flux emission (product of nuclear fusion reactions when deuterium is used as filling gas [8]), etc.

During the DPF formation ion and electron beams are accelerated within a pulse of plasma in the 0° direction [6], as it was schematized in Figure 1. The remnant of the plasma current sheath (basically composed by ions of the carrier gas) is also emitted in the 0° but with some delay following the energetic ion beams.

2.2- Diagnostic systems: external current discharge and plasma monitoring

PF discharges were studied simultaneously by Optical Emission Spectroscopy (OES) and by monitoring the external electric current discharge.

The OES system shown in figure 1, comprises a triple grating monochromator (Jarrell Ash 27 monospec) with an optical multi-channel analyzer (1024 cooled photodiodes) with a time resolution per spectrum of 30 ms (OMA III from Princeton Applied Research).

A lens-diaphragm system (external to the vacuum chamber) was used to monitor the plasma through a small glass window. The small window used was located at the end of an aluminum cylindrical conduct of 5.6 mm of diameter and 25 mm length, aligned with the focusing optical system. On one hand, this conduct permitted, the elimination of most of the light belonging from outside the studied region (improving the spatial observation resolution); and on the other, the light intensity reduction to levels which did not saturate the photodiodes storage capacity. This optical set up was focused into de DPF column, giving a spatial resolution of ~ 2 mm.

Experiments focusing the region to be studied through a 150 mm diameter window (without the aluminum conduct) showed complete saturation when the spectrometer was focused at **z** = 0, 5 and 10 mm from the end of the anode and along the DPF column, a complementary neutral filtering (10 % transmission) being necessary to reduce the intensity to observable intensity levels. Outside the DPF column region, **z** = 20 mm for example, the level of intensity was strongly reduced allowing the direct observation of the spectra (without neutral filtering), showing saturation only for the most intense emission lines. Far from the DPF region (**z** > 100

mm), the spectra intensities were strongly reduced, being observed, in addition, several bands corresponding to the presence of molecular species in the plasma. The above considerations insure that the spectra, observed through the small glass window (plus the aluminum conduct), belong almost exclusively to the DPF column region.

On the other hand, taking into account the short duration of the PF discharge (~ 3 μs) and the spectrometer sweeping time (30 ms), the spectra corresponds to a time integration over the whole discharge. Although the spectra were taken from different discharges they can be compared due to the good reproducibility of the results. The spectra were studied by inspection of their display in a computer monitor screen or by their printing.

In Figure 2 a spectrogram of a nitrogen discharge is presented. In fact, lines corresponding to all the ionization degrees that can be detected in the visible range were observed.

2.3- Pulsed plasma-ion beam characteristics

The pulsed plasma generated in each discharge had the following characteristics:

a- pulse time duration Δt variable between 200ns and 500ns;

b- ion fluence **f** variable between 10^{13} and 10^{15} ions/cm^2;

c- ions' energy spectral law: $N/E \sim E^{-2.4}$ (N number of ions with energy E) with E ranged between 20 to 500keV;

d- energetic ion beam emission (within the plasma) with a conic geometry with a solid angle of ~40°.

These energetic ions were used to study their effect on the surface of different metals and alloys by exposing specially prepared samples to the beams at different **z** distances from the **DPF** as shown in Figure 1.

Higher total fluences **F** can be obtained by means of successive pulse emission of single fluences **f**. Then the total accumulated fluence will result **F = nxf** where **n** is the number of pulses accumulated.

2.4- Plasma-surface interaction: thermal process characterization

Due to the short duration of the beam pulses, a fast energy release takes place during the ion beam interaction with solid surfaces. An evaluation of the heating process was done using finite differences calculations [9], because of the practical impossibility of measuring the

thermal evolution in the implanted layers due to the short duration of the process (~400ns) and the small region (~1μm) affected.

In Figure 3 the thermal evolution of the surface during the interaction of a nitrogen ion beam with pure titanium, are plotted versus the target depth for different times. The pulse time length is directly related with the velocity of energy deposition during ion implantation, and consequently with the heating velocities and peak temperature on the surface: the shorter the pulse time length, the higher the thermal shock.

In this case, the results for two different pulse time lengths Δt are presented. For Δt=350ns the titanium melting point is reached (part a of figure 3), whereas for Δt=400ns the peak temperature is below the melting point (part b of the figure). In addition to the high peak temperatures the calculations show the velocity of the heating process, with heating velocities of ~15K/ns and associate temperature gradients of ~1500K/μm.

Considering that the time lapse between ion beam pulses during a repetitive implantation process is ~1s, and taking into account that the surface of the target returns to room temperature in almost several tens of microseconds (see Figure 3), every new ion beam reaches the target surface completely thermally relaxed. This heating process was verified experimentally by the surface observation of implanted samples which show, in the case the shorter ion beam pulses, the damage to the surface of the target due to the material melt down.

2.5- Results of surface treatment of metals

Samples of different metals and alloys specially prepared (surface polished up to 1 micron diamond paste) were located at different distances down stream from the DPF region, with their surface perpendicular to the symmetry axis of the coaxial electrode system. They were exposed to the plasma beams under different conditions of pulse time duration (varying the distance from the DPF), total fluence **F**, and with different ion species (different filling gases).

Once exposed, they were characterized by means of different diagnostic techniques like X ray diffraction, XPS, photomicrography, etc., and studied some of their mechanical and tribological behavior modifications.

2.5.1- Steels

Different types of steels were studied under different pulsed plasma irradiation conditions. The more relevant were the austenitic AISI 304 stainless steel, the ferritic High Speed M2 type and the Auto-tempering tool steel. The results can be resumed as following:

2.5.1.1- AISI 304 stainless steel (0.08C, 1.4Mn, 0.6Si, 0.04Mo, 9.0Ni, 18.6Cr, 0.051Co, 0.057P).

There was observed a strong improvement in the wear rate (comparative results between implanted and non-implanted samples show a wear rate reduction of 90%) and a reduction in the friction force, for a nitrogen ion implantation with a total fluence $F=1.3x10^{17}$ cm^{-2} and pulse time duration $\Delta t=280ns$[10].

The nitrogen concentration profile (determined through XPS technique) of the implanted layer shows a 12at.% in the surface decreasing to 6at.% at a depth of ~10nm, maintaining this percentage constant down to the deeper layer observed, i.e. 180nm.

X-ray difractograms show the Fe_2N formation and the presence of α'-Fe (ferritic phase) in the preexisting γ-Fe (austenitic phase) of the AISI 304.

2.5.1.2- M2 type high speed steel (0.83C, 0.3Si, 5.0Mo, 4.1Cr, 0.3Mn, 1.9V, 6.1W).

Wear tests of high speed steel were done under special experimental conditions. Non-implanted and nitrogen implanted high speed steel cutting tools were wear tested in an industrial boring process of SAE 1045 parts [11].

The results showed a systematic reduction of ~50% in the wear rate, when nitrogen implanted with a total fluence $F=1.65x10^{17}$ cm^{-2}, and pulse time duration $\Delta t=280ns$. X-ray diffraction analyses showed, on the affected layers, the formation of Fe_4N, Fe_3C and NW, with the development of the γ-Fe (austenitic) phase in addition to the preexisting α-Fe (ferritic) one. However Co_3W_3C compound, observed in non-implanted samples, was totally absent after implantation being part of the source of W in the NW development. The nitrogen concentration profile after implantation (XPS measurements) showed ~22at.% at the surface, with a reduction to ~12at.% at 8nm depth, maintaining constant the percentage to the deeper levels observed (~50nm).

2.5.1.3- Auto-tempering tool steel (0.53C, 0.50Mn, 0.33Si, 3.8Ni, 1.65Cr, 0.27Mo, 0.03W, 0.17Cu, 0.01Al, 0.01P)

Samples of this material were nitrogen ion implanted with three different type of beams: **Beam 1** with a pulse time length $\Delta t=350ns$ and total fluence $F=2.6x10^{16}$ cm^{-2}, **Beam 2** with a $\Delta t=400ns$ and $F=4.2x10^{16}$ cm^{-2}, and **Beam 3** with $\Delta t=280ns$ and $F=8x10^{16}$ cm^{-2}.

Sample surfaces, before and after implantation, were observed and photographed (320X) through an optical microscope [11]. No changes (martensite) were observed for the case of implantation using **Beam 1** and **Beam 2**. Nevertheless, in the case of implantation with **Beam 3** a surface melted layer was observed.

Microhardness measurements using a 25g load, also show no changes (~270HV) both before and after implantation with **Beam 1** and **2**. Nevertheless, an important increase was observed (up to ~550HV) in cases of implantation with **Beam 3**. These results showed the influence of the thermal effect caused by the faster energy release in the **Beam 3** case.

2.5.2- Pure titanium

Pure titanium samples were nitrogen ion implanted with two different types of beams[12] which corresponds to the **Beam 1** and **Beam 2** conditions described above.

The XPS study of the implanted layers showed the titanium nitriding formation, with the stoichiometry $TiN_{0.85}$ for the implantation condition with **Beam 1**, and $TiN_{0.80}$ with **Beam 2**. The nitrogen concentration profile show, for nitrogen implanted samples with **Beam 2**, a constant value of 43 at. % in the surface layer down to a depth of ~30nm, with a gradual decrease toward deeper levels, reaching a 31 at. % at the deepest level measured, ~60nm.

The HV microhardness of non-implanted samples, and the implanted ones under both conditions (**Beam 1 or Beam 2**) were measured with a load of 5g. In the case of pure titanium the HV was 270kg/mm^2 whereas for samples implanted under both conditions, the HV was 655kg/mm^2 .

2.6- Residual stresses induced by the pulsed plasma irradiation

Using the X ray diffraction technique, the interplanar distance variation of the crystalline structure due to the existence of stresses can be determined. We use this technique to study the surface residual stress modification of the AISI 1075 steel after its irradiation with nitrogen pulsed plasmas

The results (that together with the method are fully described in reference [13]) showed the induction of a tensile stress state that varies with the depth down to 200 microns where the layers can be considered non perturbed (see figure 4).

2.7- Residual deformation induced by the pulsed beams

Using hollographyc interferometry, the residual deformations induced in surfaces irradiated by pulsed plasmas were studied. The fringe pattern obtained by the superposition of two successive holograms of the surface of the sample (different type of steels), one before and other after the plasma irradiation, gave us the state of deformation in the line of sight. We have exposed different metals (copper, aluminum, lead, titanium) and different type of steels (austenitic AISI 304 stainless steel, low carbon steel, etc.) to plasmas of nitrogen, hydrogen and argon, with different **Δt**, **f** and **F**. In all cases we fund a negative state of deformation (concave) but with magnitude that it depend on the material and the plasma pulse characteristic. The experimental method and the results were described in reference [14]

2.8- Conclusions about the process

A clear and important improvement in the tribological properties of steel and titanium were observed after nitrogen ion implantation with pulsed plasmas generated with Plasma Guns.

Nevertheless, the explanation of this structural modification has to be found not only in a pure ion implantation process, but also in the thermal effect that the fast energy release, due to the short duration of the beam pulse, induce in the first 2-3μm under the surface. This thermal effect, that it was modeled and explained in the paragraph 2.4- can be seen as the cause of:

1- The nitrogen concentration uniformity in depth observed in the irradiated materials that can not be attributed only to a single ion implantation process. The successive plasma irradiation redistribute by the thermal effect the nitrogen left by the preceding pulses.

2- In the case of titanium, the high values of nitrogen concentration observed, contrast with the low fluences used in the implantation processes. Total fluences F of $2.6x10^{16}cm^{-2}$ and $4.2x10^{16}$ cm^{-2} can not develop layers with the nitrogen concentration measured. In this case, and taking into account the getter properties of titanium, the combined effect of the strong thermal shock induced by the ion beam pulses, plus the highly activated nitrogen plasma which interact with the target immediately after the ion beam incidence, can be responsible for an extra nitrogen incorporation to the surface. The nitrogen, which is implanted with every ion beam, is redistributed with the following ion beam pulse due to the high temperatures and strong temperature gradients, conducing to more uniform and deeper nitrogen concentration layers, by a thermally assisted diffusion process. Particularly, the remaining plasma which follows the ion beam acceleration, can contribute to increase the nitrogen surface absorption.

In this regime, and for pressures of several milibars, the applied voltage is virtually translated to the region near the cathode (only 1 or 2 millimeter thick), converting the cathodic region (cathode fall) in the most active one. Is in this region where most of the plasma reactions occurs, and is there where most of the attention is concentrate to use it in process like ion nitriding, carbonitriding, etc.

3.2- Ion Nitriding

Ion Nitriding is a technique in which a glow discharge in pure nitrogen or mixture with hydrogen is produced. In this conditions, active nitrogen atoms are generated and put them in contact with the surface being absorbed by it. Once in the surface layer the atoms begin to migrate to the bulk through a diffusive process. When the nitrogen concentration grows in the material, normally phases of different nitrogen compounds are formed, like iron nitriding when for example; the steel is the material to be treated.

Our research in this field was orientated in four directions:

a- Characterization of the process in steel surface hardening

b- Study of the process as a hydrogen permeation barrier generation

c- Study of the molecular activity in the plasma during ion nitriding.

d- Problems of scale for industrial machines construction.

3.2.1- Surface characterization

Surface characterization was done using conventional methodes like: X-ray diffraction, Auger, photo - micrography, SEM, etc. These techniques were used routinely to test the processes. Nevertheless, a new technique was installed to study the phase formation and evolution *in-situ* and in *real time*. This technique is basically the X-ray diffraction, but using the X-rays from a synchrotron. The possibility to choose the wavelength appropriate for the material, depth, and type of phase to be studied, is one of the advantages. But the most relevant are the high energy associated to the beams, that allows to record a full difractogram in few minutes; and the availability of enough space to install in the X-ray beam line an ion nitriding reaction chamber.

A specialy constructed reactor (Figure 6) was installed in the SAXS beam line of the National Synchrotron Light Laboratory, Campinas (Brazil), adapted for X-ray diffraction experiments. This beam line produces a monochromatic X-ray beam using a (111) silicon crystal

reflection [15]. The beamline arm and the crystal Bragg angle were adjusted in order to have the beam hitting the sample with a wavelength λ=1.76A The silicon crystal collects 7 horizontal mrad of the incident white beam. It has a triangular shape and is bent in order to focus the beam horizontally. Adequate slits define the geometry of the beam, whose cross-section at the sample position is 6mm horizontal and 0.3 mm vertical.

The entrance and exit of X-ray beams were laterally centered with respect to the slit by a lateral chamber translation. The coincidence of the X-ray vertical beam position with the axis of sample rotation was achieved by iterative vertical translations and rotations of the sample holder, while the intensity of the direct beam is monitored using a scintillator counter located at 2θ=0.

In order to avoid additional alignments for different samples, their thickness is always kept constant and equal to 2 mm.

The angle α between the direct beam and sample surface can be selected in order to probe the sample volume at different depths. In order to maintain constant the instrumental contribution to Bragg peaks width when α is decreased, the vertical size of the direct beam should be accordingly reduced.

a- Detection system

The photons diffracted by the sample exit the reaction chamber through the Kapton window and are recorded by means of a Molecular Dynamics imaging plate. The imaging plate is placed on the surface of an external cylindrical frame (163.8mm diameter) whose axis is coincident with that of sample rotation.

The cylindrical frame containing the imaging plate can be displaced horizontally along the direction of the sample axis of rotation by mean of a translation stage driven by a stepping motor. This system is used to record many X-ray diffraction patterns (up to 16) successively. Once completed the recording of all the diffraction patterns, the imaging plate is removed from the frame and transferred to an electronic reader. Image-Quant software is used to define the width of the imaging plate area to be read and to obtain two columns data files for each pattern, corresponding to plate position and X-ray intensity. The pixel size used for the imaging plate reading was100 microns.

b- Nitriding conditions in our tests

The electric discharge across the gas inside the reactor was generated by a pulsed DC power supply. The voltage is a polarized square wave with an amplitude that may be varied from

0 to 600V. This negative potential is applied to the metallic sample holder, the rest of the chamber remaining at ground potential. The frequency can be varied from 0 (DC) to 1kHz, with a control of the ratio between the active and passive part of each cycle of discharge [16]. The current discharge is permanently controlled by means of a digital amperimeter.

In our experiments, the gas composition was 80% of nitrogen mixed with 20% of hydrogen, being maintained inside the chamber at a constant pressure of 5.6 mbar, the applied voltage 400V, the frequency 100Hz and the active to passive ratio 60%. In this work we present the results on AISI 1010 steel.

c- Experimental results

A picture showing the spatial distribution of diffracted photon density in the imaging plate corresponding to all successively recorded spectra is shown in Figure 7. Thirteen spectra were sequentially obtained, each of them with 10 min. of exposure. The corresponding series of patterns of X-ray diffraction intensity is shown in Figure 8 as a function of the de scattering angle (Intensity versus 2θ). This series of patterns contains the necessary information to characterise the kinetics of the structural transformations during the first two hours and half of ion nitriding.

The sequence of diffractograms are indicated as: a-1, a-2,..., a-13. The first diffractogram (a-1) corresponds to the material before the beginning of the nitriding process, a normalized AISI 1010 steel.

The diffraction pattern a-1 (Figure 8) corresponds to the initial AISI 1010 steel before starting the ion nitriding process. This ferritic steel has a known bcc lattice with a parameter at room temperature a=2.87Å. Two sharp peaks at $2\theta=51.47^{\circ}$ and $2\theta=75.61^{\circ}$ are apparent in Figure 8, corresponding to Bragg reflections (110) and (200), respectively. The final state of the sample is characterized by the last diffraction pattern a-13, which was recorded between 2 hours and 20 minutes and 2 hours and 30 minutes after starting the nitriding process, with the sample at 410°C. In this pattern the 110 and 200 reflections, corresponding to the Fe-α phase, are still visible but somewhat attenuated.

In addition to the Bragg peaks corresponding to the parent Fe-α phase, a number of others are apparent in pattern a-13. They were identified as produced by several different iron nitrides. We identified the 110, 111, 200, 210, 211 and 220 reflections as produced by a Fe_4N-γ''phase. Two peaks detected (100 and 102) were attributed to a $Fe_{3+x}N_{1-x}$-ε phase with x=0.17 [17].

The pattern a-3 was taken between 23 and 33 minutes of process with a final temperature of 395°C. A comparison between a-3 and a-2 indicates that all peaks corresponding to the different nitrides strongly increase as the process evolves. In addition, in the particular case of the peak corresponding to the Fe_3N-ε phase, the angular position shifts toward 2ϑ=49.93°. Beside the mentioned peaks, others appear at 2θ angles of 43.77°, 65.88° and 80.08° corresponding to the hexagonal 100, 102 and 110 reflections from the Fe_3N-ε phase, at 44.82° related to the 100 reflection from a $Fe_{3.17}N_{0.83}$-ε phase and at 62.3° associated to the 210 reflection from a Fe_4N-γ phase.

The shift in the angular position of some of the peaks toward higher 2θ angles from a-2 to a-3, was also observed in patterns a-4, a-5 and a-6. This behavior is illustrated in table II, which reports the 2θ angles and the corresponding d_{hkl} values corresponding to the different phases.

The variation in peak positions, indicating a progressive decrease in interplanar distances during the first minutes of nitriding treatment, only occurs to hkl reflections corresponding to the Fe_3N phase and not to all the others, even not those associated to $Fe_{3.17}N_{0.83}$-ε, a phase with nearly the same stoichiometry.

Analyzing, in particular the case of the Fe_3N-ε phase, we remark that the angle associated to the 111 reflection in the a-2 pattern leads to a value of the interplanar distance d_{101}=1.1523 Å. This value is larger than that corresponding to the a-3 pattern, d_{101}=1.1499Å, even though that a-3 pattern was recorded with the sample at a higher temperature.

The decreasing trend of d_{hkl} values corresponding to the Fe_3N phase is maintained for a-4 and a-5 and then approaches to a nearly constant value (within the experimental errors) of d_{hkl} = 1.1464Å. Considering that the d_{101} modification for t>17 min takes place for almost a constant temperature, this variation in interplanar distance cannot be attributed to thermal effects. The variations in d_{101} corresponds to a relative linear expansion of 0.52% (17 min), 0.31% (28 min) and 0.011% (38 min) with respect to the final state. This suggest that the initial Fe_3N phase is subjected to stresses producing a significant volume expansion which is progressively relaxed during the nearly isothermal conditions of the advanced stages of the nitriding process.

The particular behavior observed for Fe_3N seems to be exclusive to this phase because the interplanar distances corresponding to the others, even $Fe_{3.17}N_{0.83}$-ε remain constant from t= 17 min until the end of the process, as can be seen also in Table I.

Table I. Angular possition (Bragg angles) of the Fe_3N-ε (44.82°) and $Fe_{3.17}N_{0.83}$-ε phases for different treatment times.

PHASES	2θ / d_{hkl} Å							
	a-1	a-2	a-3	a-4	a-5	a-6	...	a-13
Fe_3N (100)	------	------	43.77°	43.91°	44.98°	44.98°	...	43.91°
			2.3609	*2.3537*	*2.3005*	*2.3005*		*2.3537*
$Fe_{3.17}N_{0.83}$ (100)	------	------	44.82°	44.75°	44.89°	44.75°	...	44.68°
			2.3083	*2.3117*	*2.3049*	*2.3117*		*2.3152*
Fe_3N (101)	------	49.79°	49.93°	50.07°	50.14°	50.07°	...	50.14°
		2.0905	*2.0850*	*2.0795*	*2.0768*	*2.0795*		*2.0768*
Fe_3N (102)	------	------	65.88°	66.02°	66.16°	66.16°	...	66.23°
			1.6184	*1.6153*	*1.6123*	*1.6123*		*1.6108*
$Fe_{3.17}N_{0.83}$ (102)	------	------	------	------	------	------	...	67.28°
								1.5885
Fe_3N (110)	------	------	80.08°	80.29°	80.36°	80.50°	...	80.50°
			1.3679	*1.3649*	*1.3639*	*1.3620*		*1.3620*

3.2.2- Hydrogen permeation modification of steel by surface ion nitriding

Using the same parameter of ion nitriding that the ones described in 3.2.2.1-, samples of API 5L X-65 steel were treated for hydrogen permeation tests. The permeation tests were performed in the Hydrogen Lab. of the Metallurgical Department of the University of Rio de Janeiro, Brazil.

Hydrogen permeation parameters were determined using electrochemical hydrogen permeation tests, the necessary cathodic charging potentials being obtained from the results of prior potentiodynamic polarisation scans. All electrochemical tests were performed using a TAI GP-201H programmable electrochemical interface (galvanostat/potentiostat/zero resistance

ammeter) which permitted fully automated control and on-line monitoring of all test parameters as well as data acquisition via microcomputer. Details of this technique and equipment can be found in references [18,19].

The hydrogen permeation tests were undertaken utilising a two-compartment electrochemical cell (one for hydrogen generation and the other for hydrogen detection) both containing 0.1N NaOH electrolyte solution. Thermostatic control of the cell maintained a temperature of 50°C throughout the tests. Cathodic hydrogen generation potentials of 1.30 V/SCE and 1.36 V/SCE were used for the untreated and nitrided samples, respectively.

In the permeation test, the sample, of 13 mm diameter and 1 mm thickness is positioned between the two compartments and a constant cathodic potential is applied in the generation compartment. In the detection compartment, potentiostatic control is maintained at a level equivalent to that of the open circuit (to oxidise hydrogen arriving at the sample surface after permeating through from the generation side). Since the current required to maintain a constant detection potential is proportional to the flux of hydrogen which permeates through the sample, the analysis, via Fick's laws, of a curve plotting the evolution of this current with time permits the determination of the permeability, diffusivity and solubility of hydrogen in the material under test.

Tests were undertaken on samples of the API 5L X-65 steel in the untreated and in the 6 h plasma nitrided conditions. In the latter case tests were performed for two distinct sample orientations; with hydrogen charging via the nitrided face, and hydrogen charging via the non-treated face of a nitrided sample.

a- Characterization of the treated surface.

The results of the surface modification showed (grazing X-ray diffraction technique) peaks due to the γ'nitride Fe_4N and the ε nitride $Fe_2N_{(1-x)}$. The SEM analysis of transversal cuts of nitrided samples showed a surface (γ'+ ε) nitride layer (as indicated by the x-ray difraction results) of around 2 μm thickness, as well as an intragranular acicular phase typical of $Fe_{16}N_2$ in such materials.. The presence of this acicular phase was only observed up to depths of around 20 μm, in the material bulk.

Micro hardness determinations (Knoop hardness) showed for the base material values in the range 150 to 220, whereas the 2 μm nitrided surface layer was much harder with values ranging from around 600 to over 1200, with an average of 870. Immediately below the nitride

layer, the Knoop hardness was found to be in the range 280 to 360. By a depth of 250 μm it was approaching the base metal hardness, further decreasing gradually until, at around 550 μm the hardness was equal to that at the untreated face and in the sample bulk.

Then we can conclude that the 6 hour pulsed plasma nitriding treatment produced a 2 μm thick surface nitride layer containing both γ' (Fe_4N) and ε ($Fe_{2-3}N$) nitrides, as well as precipitation of α'' ($Fe_{16}N_2$) up to a depth of 25 μm.

b- Hydrogen permeation results

The hydrogen permeation curves are presented in figure 9. A marked difference is evident between the curves corresponding to the plasma nitrided samples and that for the untreated material, the nitriding treatment having provoked a significant reduction in the hydrogen permeability. Table II presents the calculated hydrogen permeation parameters.

Table II

Hydrogen permeation parameters calculated for the API 5L X-65 steel from the data presented in figure 9.

Material	Plasma Nitriding Time (h)	Diffusion Coefficient (D) ($m^2.s^{-1}$)	Hydrogen Solubility (S) (mol H. m^{-3})	Steady State Hydrogen Permeability (P∞) (mol H. $m^{-1}.s^{-1}$)
Untreated Steel	—	$D_s=1,56 \times 10^{-10}$	$S_s=1,9$	$P_{\infty S}=2,97 \times 10^{-10}$
Nitrided Steel	6	-	-	$P_{\infty ns}=7,1 \times 10^{-11}$ $P_{\infty sn}=3,8 \times 10^{-13}$

The surface nitride layer is responsible for the very significant reduction in the kinetics of hydrogen permeation in plasma nitrided steels, rather than the nitrogen saturated ferrite in the sub-surface diffusion layer. In this study it was reduced from 2.97×10^{-10} to 7.1×10^{-11} mol H. $m^{-1}.s^{-1}$. The face centred cubic structure of the γ' in particular was found to exhibit a much higher hydrogen solubility and much lower hydrogen diffusivity than the body centred cubic ferrite. The nitride layer, therefore, acts as an efficient hydrogen diffusion barrier. When the nitride layer is positioned on the hydrogen detection side of the electrochemical cell the hydrogen permeability is further decreased to 3.9×10^{-13} mol H. m^{-1} s^{-1}. This may be explained by the fact

that with this experimental orientation the rate controlling step is the low hydrogen diffusivity of the nitride layer. A complete description of our results are presented in references [20] and [21]

3.2.3- Plasma characterization

The plasma characterization in the cathodic region is of interest because the evolution of the active species can give the necessary information to the process of ion nitriding modelization. In our case, the use of pulsed discharges (square wave) introduces a new incognito: the role of the after glow in the process. Traditionally, the use of pulse discharges instead of DC was done principally because reduces drastically the risk of spark production during the ion nitriding process. The spark production is not desirable because causes concentrate damage in the surface, with the reduction in the surface smothness requirements (principally in industrial applications).

To study the species production and time evolution, the real time optical emission spectroscopy was used.

3.2.4- Experimental set up

A schematic illustration of the nitriding plasma reactor is shown in Figure 10. The reactor consists of a Pyrex/glass chamber (7 cm in diameter; 29 cm in height) wherein a stainless steel puck (3 cm diameter) at ground potential is used as the anode. The discharge is generated at a negatively biased, inverted cathode (0.6 cm thick; 3.5 cm diameter; total surface area 25 cm^2) which is centred within the reactor and parallel to the anode. The cathode is fitted with a thermocouple to monitor its temperature. The regime of operation is maily the same than the other described before.

Prior to introducing the process gases, the chamber is evacuated to a base-pressure of 15 mTorr. Using flowing N_2, an abnormal D.C. pulsed plasma is produced at a pressure between 0.5 and 10 Torr and discharge currents between 10 and 200 mA. The pulsed widths of the discharge are variable between 1 and 60 ms, where the total time available for the discharge and afterglow is the operating frequency of the power supply (16.67 Hz).

A PAR optical spectrometer (focal length 275 mm; grating width 600 gr/mm) and OMA III multichannel analyser (Princeton Applied Research) detect via an optical lens the plasma glow near the cathode. By imaging the plasma glow on the entrance slit of the spectrometer, the total discharge emission in the negative glow or in the afterglow is detected from a distance of about 1 cm from the cathode surface with an integrated time of 30 ms.

3.2.5- Experimental results

a- Emission in the N_2 discharge

The emission of the N_2 discharge is mainly produced from the negative glow around the steel cathode. The dominant specie bands are the first negative bands of N_2^+, and the first positive and second positive bands of N_2. A part of the spectrum showing emission from N_2^+ (B,0-X,0), 391.44 nm; N_2 (C,v'-B,v''), $\Delta v = -2$ and $\Delta v = -3$ bands, is shown in Figure 11 for a 4 Torr, 150 mA discharge of 30 ms duration. It can be seen in figure 10 that the N_2^+ first negative band at 391.44 nm is the most intense which is a characteristic of N_2 negative glow [22].

3.2.6- Emission in the N_2 afterglow

The N_2^+ (B-X) and N_2 (C-B) bands are always emitted in the afterglow. As the time constant of OMA detection is 30 ms, the discharge time was reduced to 18 ms to leave 42 ms to record the afterglow with acquisition times starting from 1 to 12 ms. The temporal variations of N_2^+ (391.44 nm) and N_2 (380.49 and 375.54 nm) band intensities are shown in Figure 12 for the discharge conditions of Figure 9. In Figure 10 a sharp linear decrease of the N_2^+ intensity is observed during the first 10 ms within the afterglow. The same time variations were observed for the other discharge conditions (1 and 2 Torr).

In contrast, the N_2 intensities decrease slowly with time inside the afterglow. The vibrational excitation between these bands is shown in Figure 13 which gives the I(C,1-B,3)/I(C,0-B,2) and I(C,1-B,4)/I(C,0-B,3) intensity ratios during the discharge, as well as during the afterglow as a function of acquisition start time. It can be observed that the vibrational excitation is higher within the afterglow. Similar results were obtained for experiments under the condition of 2 Torr, 80 mA, at a time up to 12 ms.

3.2.7- Kinetic analysis of the experimental results

a- Discharge conditions

From previous kinetic analyses [22,23] it can be estimated that the N_2 (C,v') excited states in the negative glow are mainly produced by electronic collisions as follows:

$$e + N_2(X,v) \rightarrow e + N_2(C,v') \qquad (a)$$

Other processes, in addition to reaction (a), can arise from collisions between N_2 (A) and N_2 (X,v) metastable molecules as follows:

$N_2(A) + N_2(A) \rightarrow N_2(C,v') + N_2(X)$ (b)

$N_2(A) + N_2(X,v>19) \rightarrow N_2(C,v') + N_2(X)$ (c)

$N_2(X,v>24) + N_2(X,v>24) \rightarrow N_2(C,v') + N_2(X)$ (d)

For reactions (b) to (d), the N_2 (C,v') populations deviate from a Boltzmann distribution and could explain the overpopulation of N_2 (C,v'=1) observed.

Considering the population of N_2^+ (B) states, it has been previously shown [24] in HF discharge and in positive column that for $n_0R > 10^{16}$ cm^{-2} (n_0 = gas density, R = tube radius), the main electron excitation is from N_2^+ ions as follows:

$e + N_2^+(X) \rightarrow e + N_2^+(B)$ (e)

with a rate coefficient $k_e = 4 \times 10^{-11}$ cm^3 s^{-1} at $T_e = 3$ eV [9].

Also, collisions with N_2 (X,v) molecules can be relevant as given by the following reaction:

$N_2(X,v>12) + N_2^+(X) \rightarrow N_2(X,v) + N_2^+(B)$ (f)

The N_2^+ (B) states are destroyed by radiative emission and quenching [25, p.122]

b- Afterglow conditions

During the afterglow the electron energy is not sustained by the plasma electric field. Only superelastic collisions at low energies are present [26]. From reference [23], a mean electron temperature of 0.5 eV has been estimated in the post-discharge. Consequently, electronic excitations having high activation thresholds such as N_2 (C) (~11 eV) are unlikely to contribute, and it can be assumed that reaction (a) disappears in the afterglow. Therefore the N_2 (C) states are mainly produced by the reactions (b) to (d).

Whereas the N_2 (A) states are quickly destroyed by collisions with the tube wall but not the N_2 (X,v) vibrational molecules [25, p.47], it is estimated that the N_2 (X,v>24) vibrational molecules are more populated than N_2 (A) in the afterglow. Through kinetic analysis it can be demostrated the nearly constant density of N_2 (C) states as presently observed in the afterglow. The N_2 (X,v) high vibrational levels coming from the afterglow could favour the following step-wise process at the beginning of the next discharge pulse:

$e + N_2(X,v) \rightarrow 2e + N_2^+$ (g)

$$e + N_2 (X,v) \rightarrow e + N + N \qquad (h)$$

The low excitation threshold of reaction (e) (2.5 eV) may permit electronic excitation of $N_2^+(B)$ states in the afterglow ($k_e = 10^{-11}$ cm^3 s^{-1} at T_e=1 eV [9]). The time varying behaviour of $N_2^+(B)$ is sharply affected by the following electron-ion recombination:

$$N_2^+ + e \rightarrow N + N \qquad (i)$$

The recombination reaction (i) is an efficient loss process which is accelerated as the electron energy decreases. This mechanism can explain the decrease of N_2^+ (B) intensity as it is presently observed.

d- Conclusion

Under conditions of N_2 pressures between 1 and 4 Torr, and current densities from 1-6 mA/cm^2, a higher vivrational excitation of the $N_2(C,v'=1)$ state has been found on going from discharge to afterglow conditions. Such an increase in vibrational excitation during the afterglow can be explained in terms of a decrease in the vibrational quenching of $N_2(X,v)$ by the neutral gas as the gas temperature is decreasing. An increase in N_2 $(C,v'=1)$ is related to an increase in the $N_2(X,v)$ vibrational population and then of N atoms which are produced by dissociation following the $N_2(v'\text{-}v'')$ climb-up process.

The excitation of N_2^+ has been analysed as occurring by electronic collisions with N_2^+ ions in the discharge and afterglow. Such an excitation is efficient in the discharge but quickly decreases in the afterglow by electron-ion recombination.

A consequence of a high level of N_2 vibrational excitation during the afterglow is to favour nitrogen ionisation and dissociation during the pulsed discharge. Then, for a given discharge current, the maintenance voltage is lowered by the stepwise ionisation process with the advantages that, first, the power yield of the plasma reactor is increased and second, the arc formation producing damage on the cathode is avoided.

3.2.4- Industrial ion nitriding reactor

Using some of the obtained results of our research an ion nitriding reactor for an industry of the region of Rosario was designed and constructed. The reactor is of 1 cubic meter of capacity with independent external heating. The power supply is a pulsed square wave varying voltage, with the possibility of frequency and the glow/afterglow ratio modification during the

process. The pulsed nature of the power supply gives the advantage of the benefits in the effective power reduction and the almost nonexistence of sparking problems.

The reactor is being used principally in surface treatment of matrixes and dies (for plastic and aluminum injection) and different parts of mechanisms and machines like gear, axle boxes, rolling, bearings etc.

In Figure 14, the reaction chamber of the reactor can be seen. In Figure 15, several pieces can be seen inside the chamber during their treatment.

4- Acknowledgments

The results presented in this work have been done in collaboration with researcher of other laboratories. I am thanksfull to A. Ricard (Centre de Physique des Plasmas et de leur Applications de Toulouse (UPRA), Université Paul Sabatier, Toulouse, France), A Craievich (Laboratorio de Luz Syncrotron, Campinas, Brasil), J. Lesage (Groupe d'Endommagement /Surfaces, Laboratoire de Mécanique de Lille URA, CNRS, France), P. Miranda (COPPE, Universidad Federal de Rio de Janeiro, Brasil), A. Costa (Universidad Federal de Ouro Preto, Brasil). Also I am thanksfull to my collaborators of the Plasma Physics Group of the Rosario Institute of Physics: E. Llonch, G. Sanchez, G. Grigioni, S. Bruhl, B. Gomez and A. Marenzana.

5- References

[1] I.J.R.Baumvol. "Ion Implantation Metalurgy", Ion Implantation Equipment and Technology, Academic Press, New York (1984).

[2] N.J.Mikkelsen and C.A.Straede. Surface and Coatings Tecnology, **51**, 152 (1992).

[3] J.Piekoszewski, Z.Werner, J.Lagner, L.Jakubowski, C.Pochrybniak and A.Harasiewicz. Nuclear Instruments and Methods, **209/210**, 477 (1983).

[4] W.Bostick, V.Nardi, W.Prior. Annals of the New York Academy of Sciences, **2**, 251 (1975).

[5] K. D. Ware, A. H. Williams and R. W. Clark, Bull. Amer. Ph. Soc., **18**,1364 (1973).

[6] J. Feugeas, E. Llonch C. O. De Gonzalez and G. Galambos. J. Appl. Phys. **64,** 2648 (1988)

[7] V. Nardi W. Bostick J. Feugeas W. Prior and C. Cortesse. Nuclear Fusion, **Suppl.2,** 143-157 (1979).

[8] K. Bergmann and R. Lebert, J. Phys. D: Appl. Phys. **28,** 1579-1587 (1995).

[9] G. Sánchez and J. Feugeas. J. Phys. D: Appl. Phys. **30 (6),** 927-936 (1997).

[10] J.Feugeas, E.Llonch, C.O. de Gonzalez and G.Galambos. J. Appl. Phys., **64**, 2648 (1988).

[11] J N Feugeas, G Grigioni, G Sánchez and A R da Costa. Surface Engineering, **14 (1)**, 62 (1998).

[12] J.Feugeas G.Sanchez C.O. de Gonzalez J. Hermida y G.Scordia. Radiation Effects and Defects in Solids, **128**, 267 (1994).

[13] A.A.Pochettino J.Feugeas M.Ortiz and G.Sanchez. Proc. 3rd. International Conference on Residual Stresses. ICRS-3 Tokushima Japan. Ed. by H. Fujiwara T. Abe and K. Tanaka Elsevier Applied Science, pg. 833 (1992).

[14] S.Brühl G.Sanchez M.Storti A.Cardona J.Feugeas and G.Kaufmann. Journal of Physics D: Applied Physics, **28,** 1655-1660 (1995)

[15] Kellermann G., Vicentin F., Tamura E., Rocha M., Tolentino H., Barbosa A., Craievich A. And Torriani I., J. Appl. Crystallogr. **30**, 880 (1997).

[16] Bruhl S., Russell M., Gomez B., Grigioni G., Feugeas J. and Ricard A., J. Appl. Phys. **30** 2917 (1997)

[17] Inokuty I., Nishida N. And Ohashi N., Metal Trans. **A6** 773 (1975).

[18] Zampronio M., Bartier O., Chicot D., Lesage J. and Miranda P., Deffect Diffusion Forum **143-147** 939 (1997).

[19] Miranda P. and Fassini F., J. Mater. Sci. **28** 5148 (1993)

[20] Bott A., Bruhl S., Gomez B., Zampronio M., Miranda P. and Feugeas J., J. Appl. Phys. **31** 3469 (1998)

[21] Bruzzoni P., Bruhl S., Gomez B., Nosei L., Ortiz M. and Feugeas J., Surface Coat. Tech. **110** 13 (1998)

[22] Petitjean L and Ricard A., J. Phys. D: Appl. Phys. **17** 919 (1984)

[23] Hugon R, Fabry M and Henrion G J. Phys. D: Appl. Phys. **29** 761 (1996)

[24] Crandall D H et al. Phys. Rev. *A* **9** 2545 (1974)

[25] Ricard A, Reactive Plasmas (SFV Edition) (1996)

[26] Capitelli M, Gorse C and Ricard A J. Physique-Lettres **42** 469 (1981)

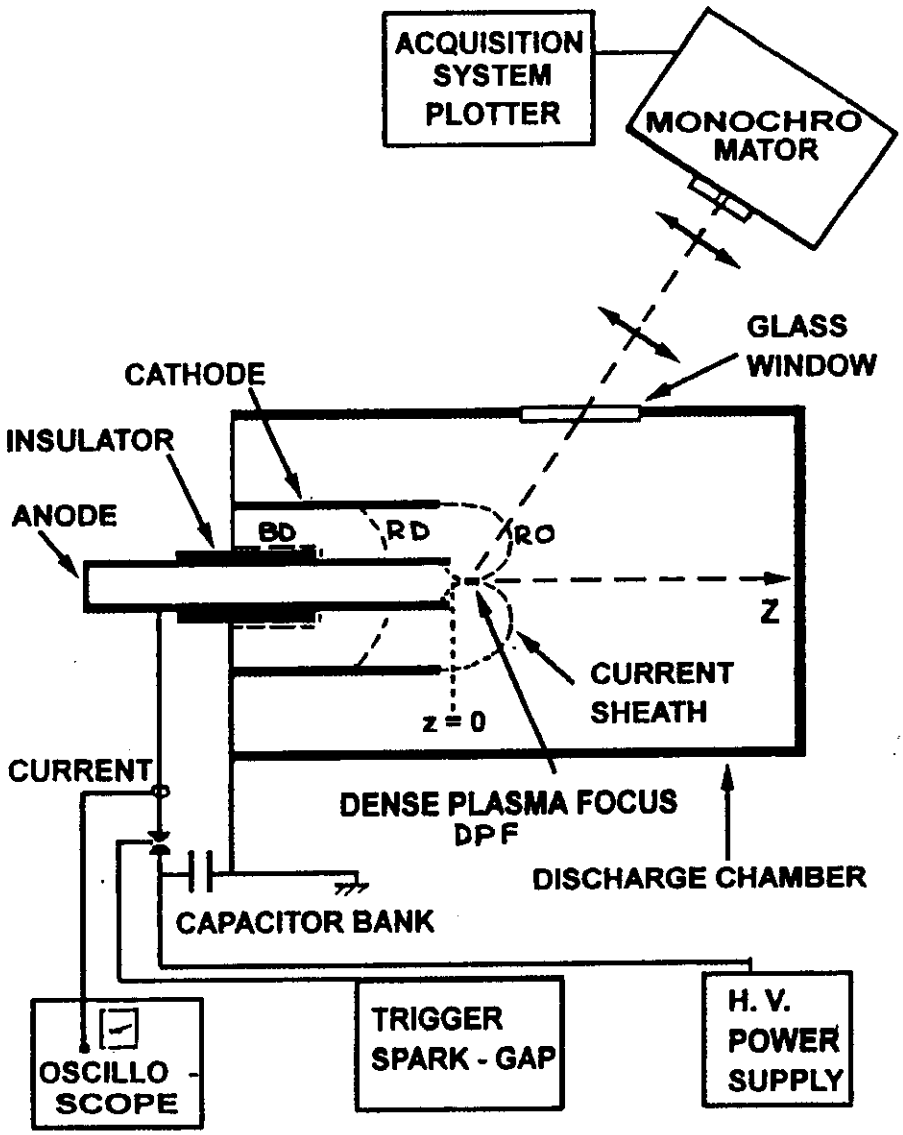

Fig.1 a) Plasma Focus: Diagram of the experimental set up and details of the discharge evolution and *pinch* formation. Stages of the current sheath: **BD**: break down; **RD**: run down; **RO**: roll of, **DPF**: pinch formation (dense plasma focus column). The spectra acquisition system (OMA) is represented in the figure.

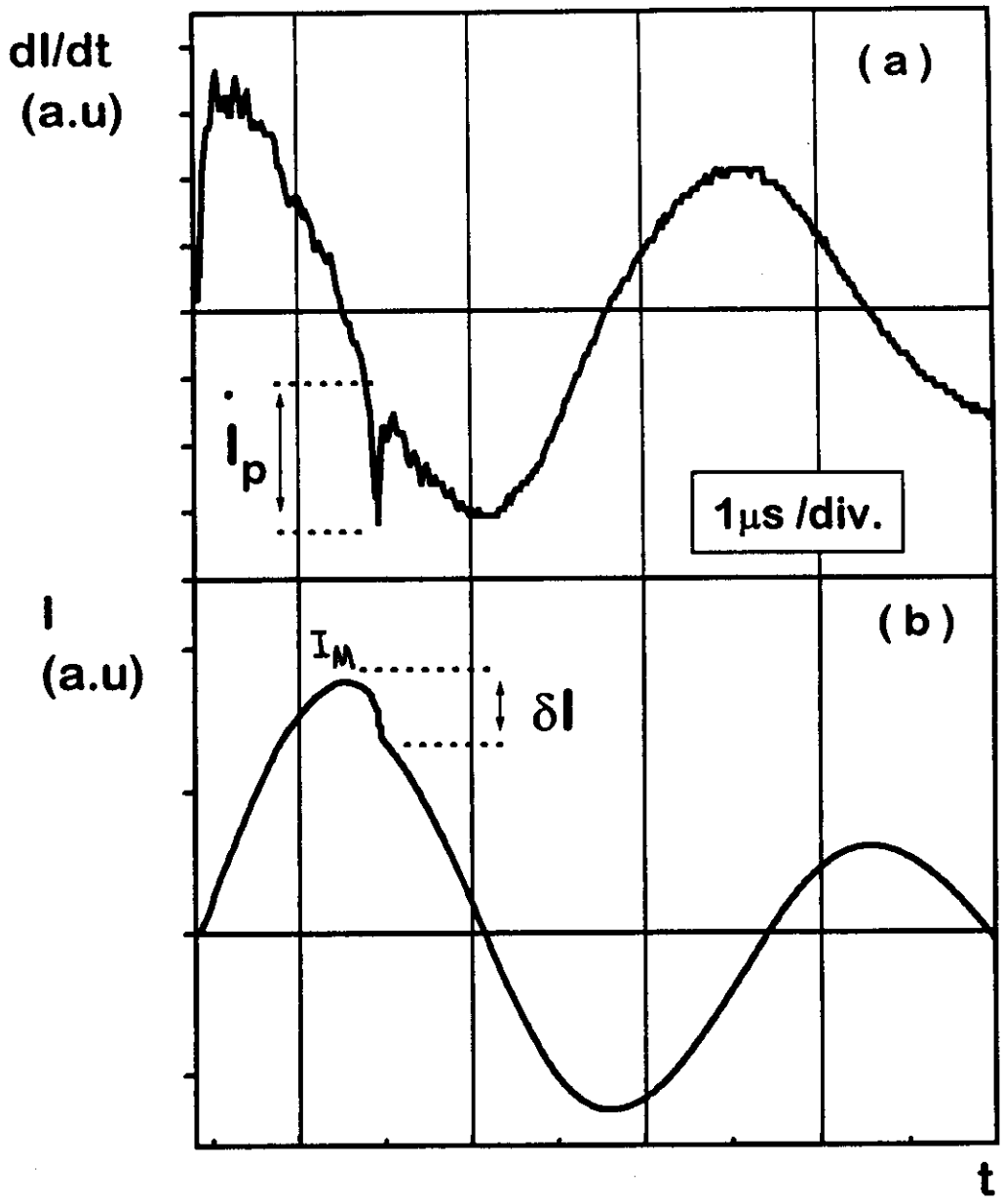

Fig.1 b) Typical traces of the external current discharge: *dI/dt* as recorded in the oscilloscope (uper trace), and the *I(t)* as integration of the *dt/dt* (lower trace).

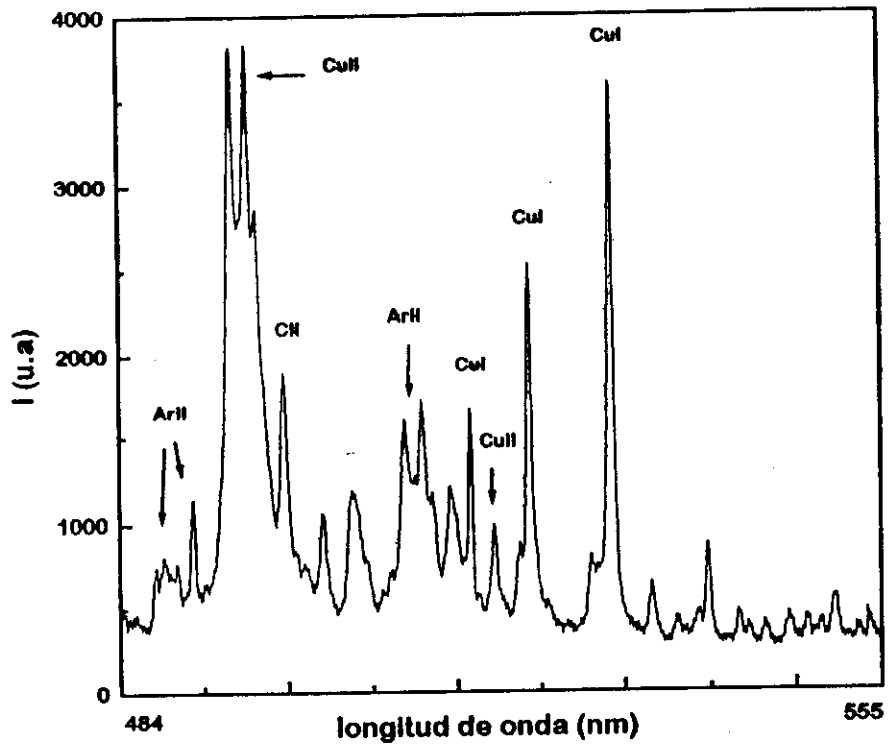

Fig.2: A typical spectrogram obtained focusing the spectroscope in the DPF region (time integrated spectrogram)

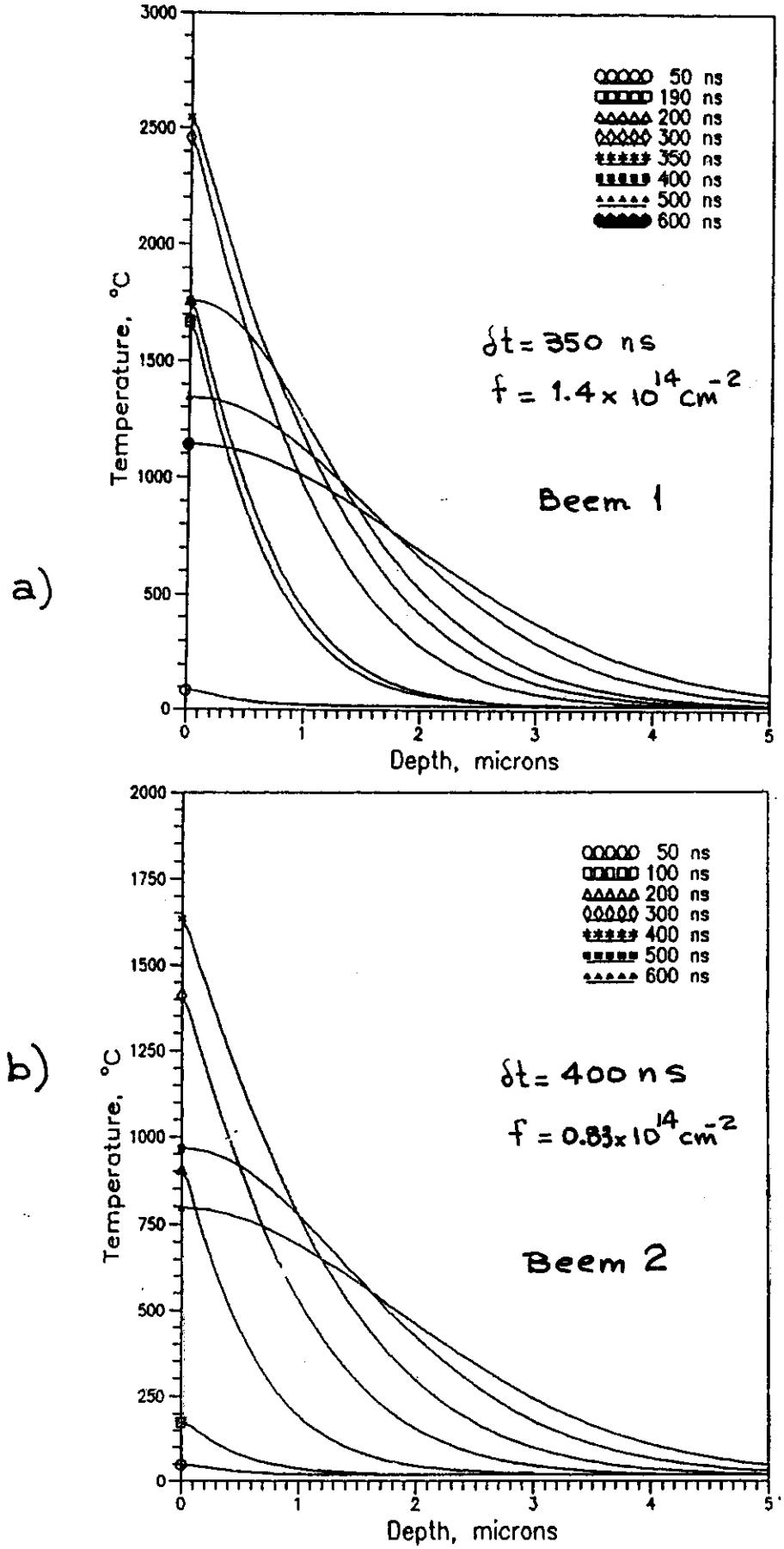

Fig.3: Temperature profiles evolution in time during the incidence of a plasma beam on pure titanium (finite difference calculations). **a-** results for a nitrogen plasma beam of 350ns time duration; and **b-** for 400ns.

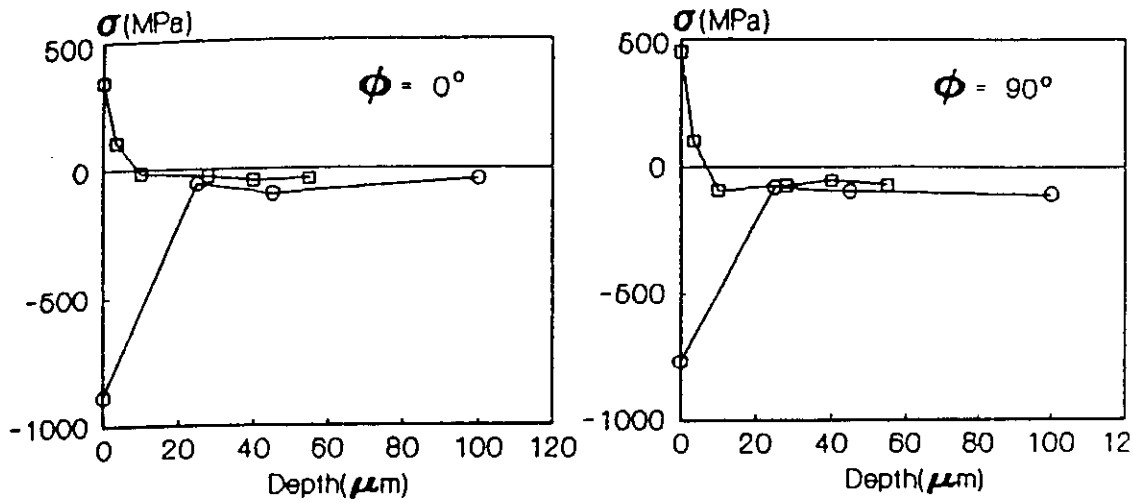

(a) Rolling Direction (b) Transversal Direction

Fig.4: Residual stresses induced on steel surface after being irradiated with pulses of nitrogen plasma.

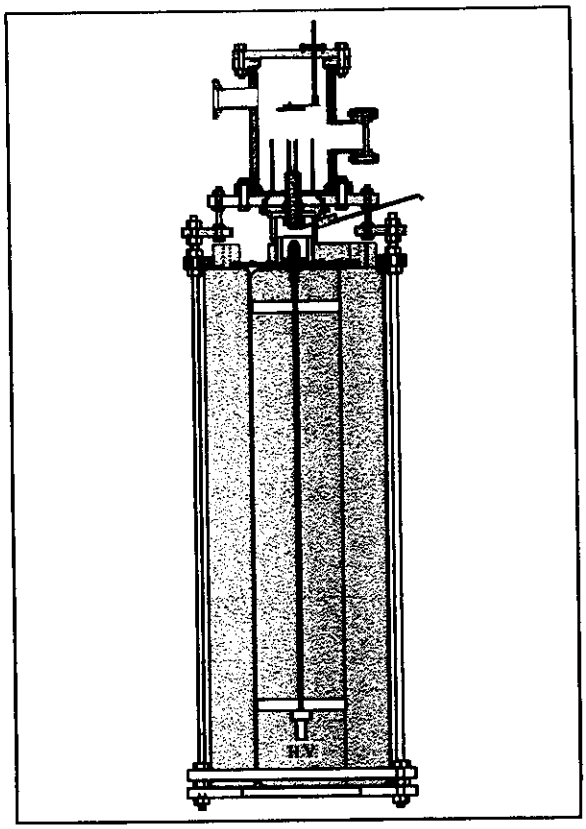

a)

b)

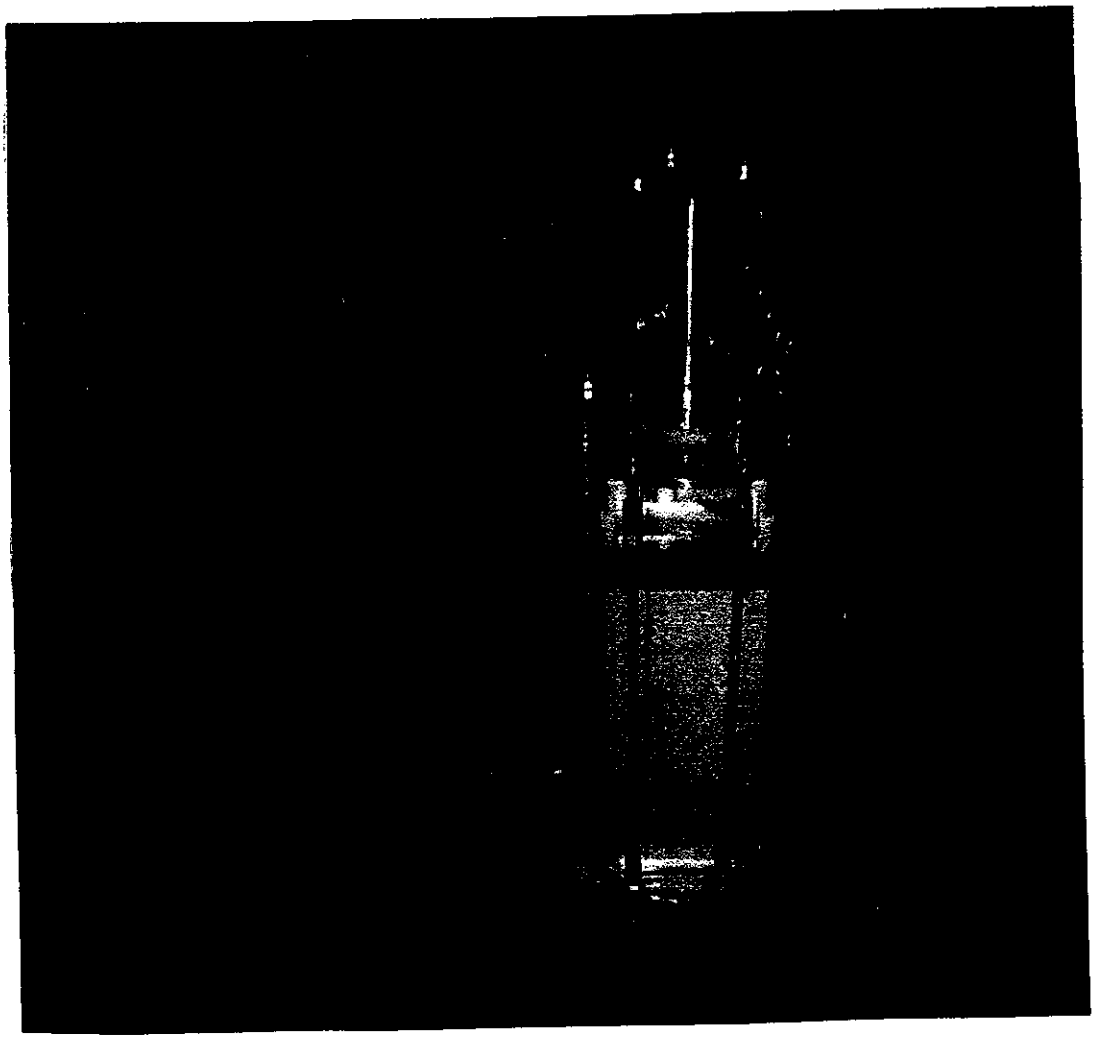

Fig.5 **a)** Compact module design and **b)** photograph of the module once finished. Part **c)** shows a typical *dI/dt* trace of the external current discharge.

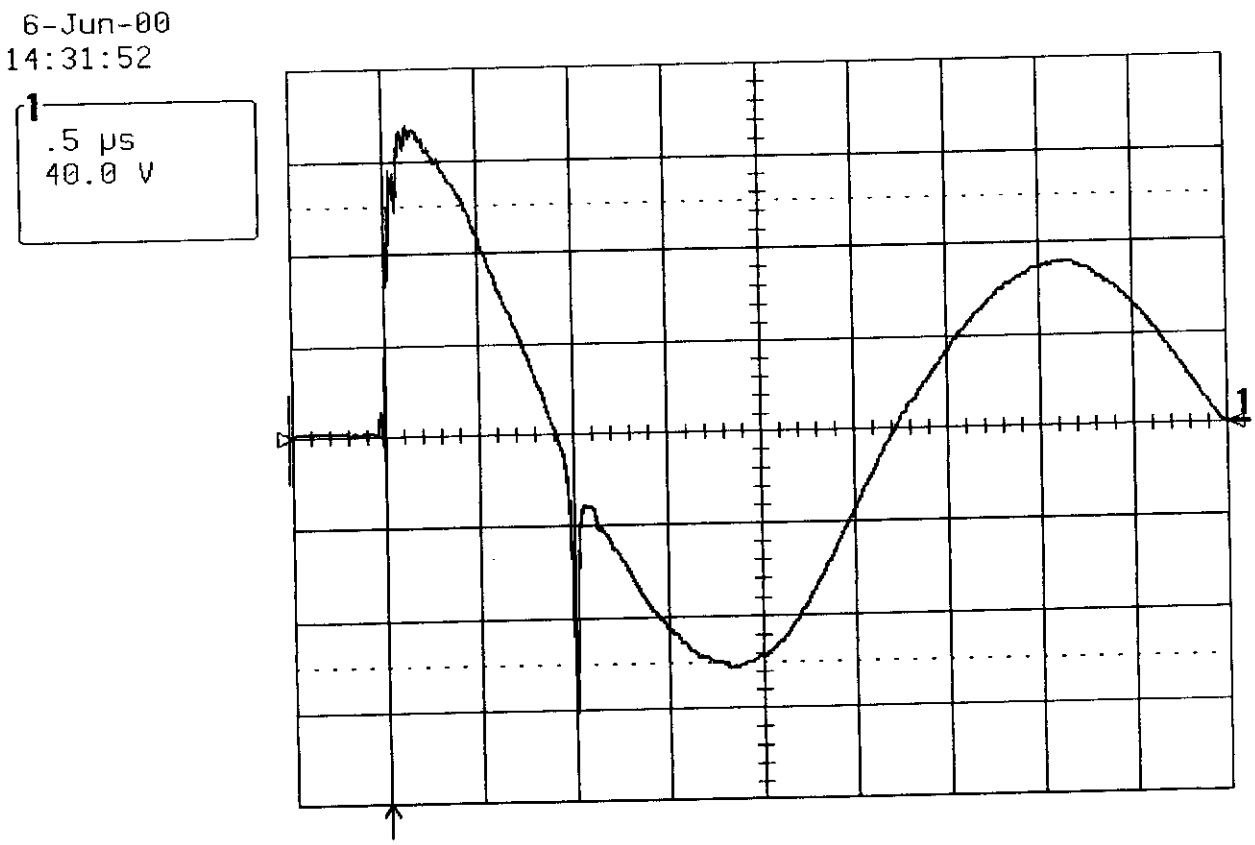

c)

dI/dt oscilloscope trace of a plasma focus discharge in nitrogen at 0.2 mbar

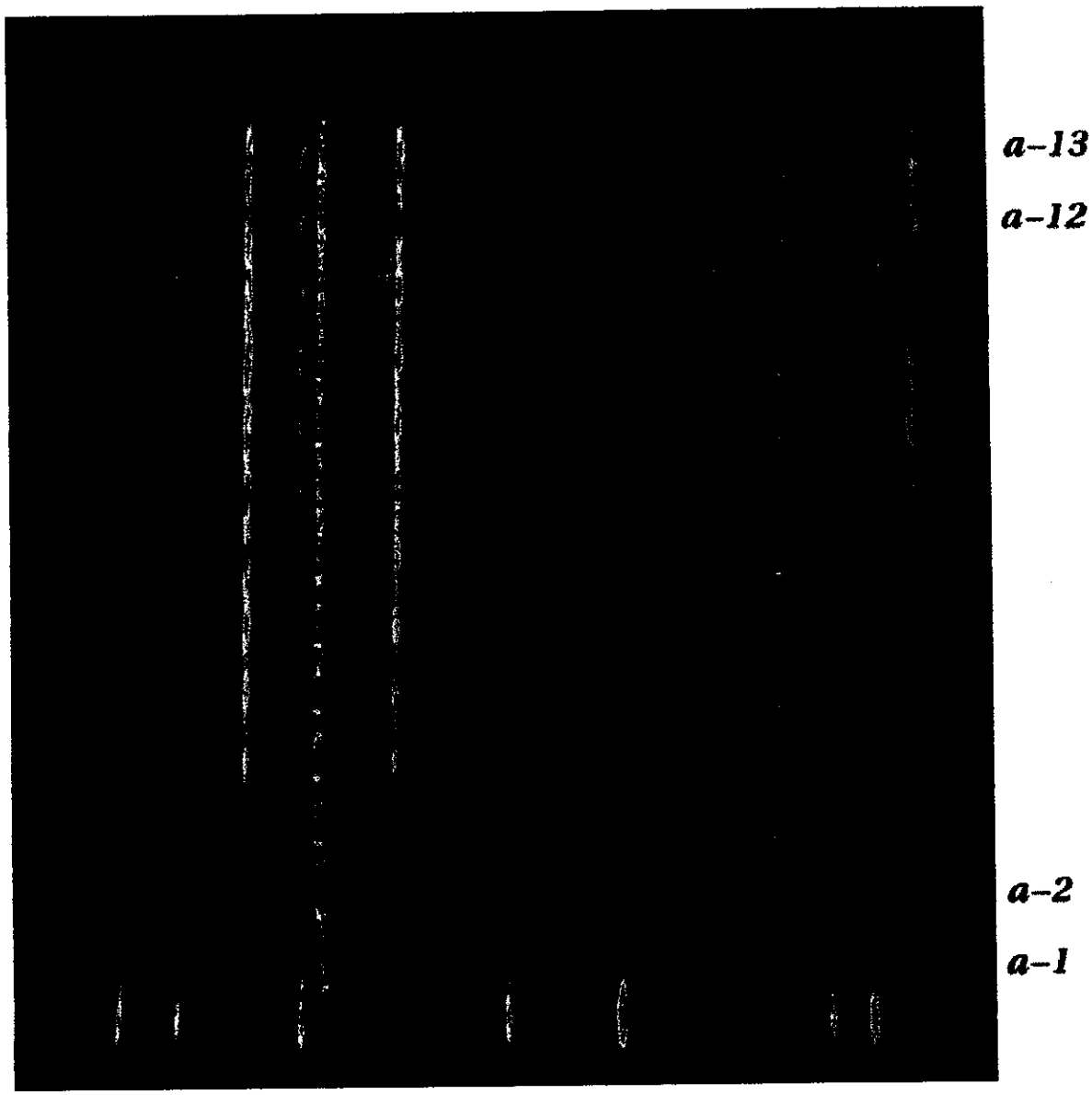

Fig. 7: Imaging Plate corresponding to AISI 1010 ion nitriding test.

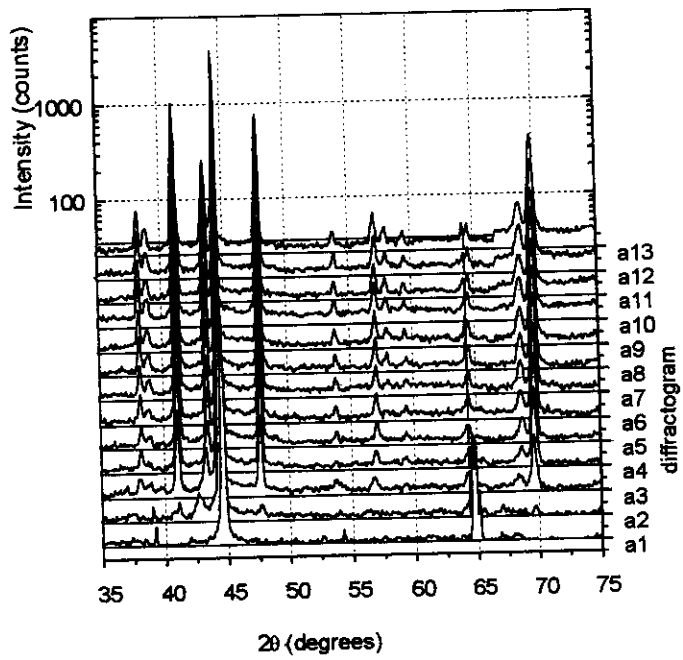

Fig.8: Sequence of diffractograms corresponding to the IP of Fig. 7.

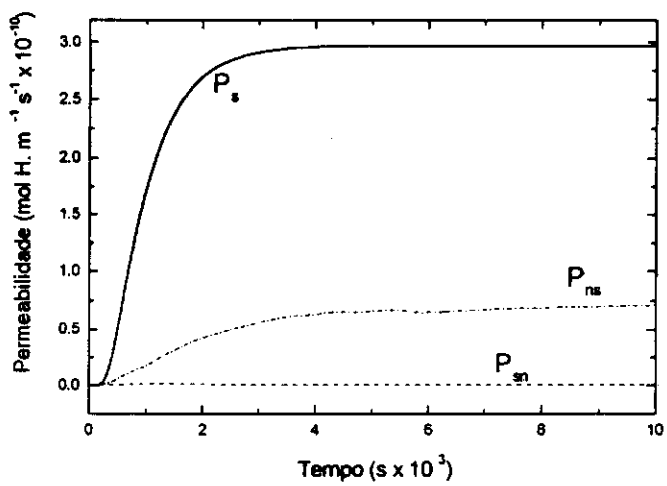

Fig. 9: Hydrogen permeation curves for the API 5L X-65 steel: P_s is an untreated sample; P_{ns} is an irradiated sample tested with the hydrogen generation in the treated face; P_{sn} is an irradiated sample tested with the hydrogen generation in the non treated face of the sample.

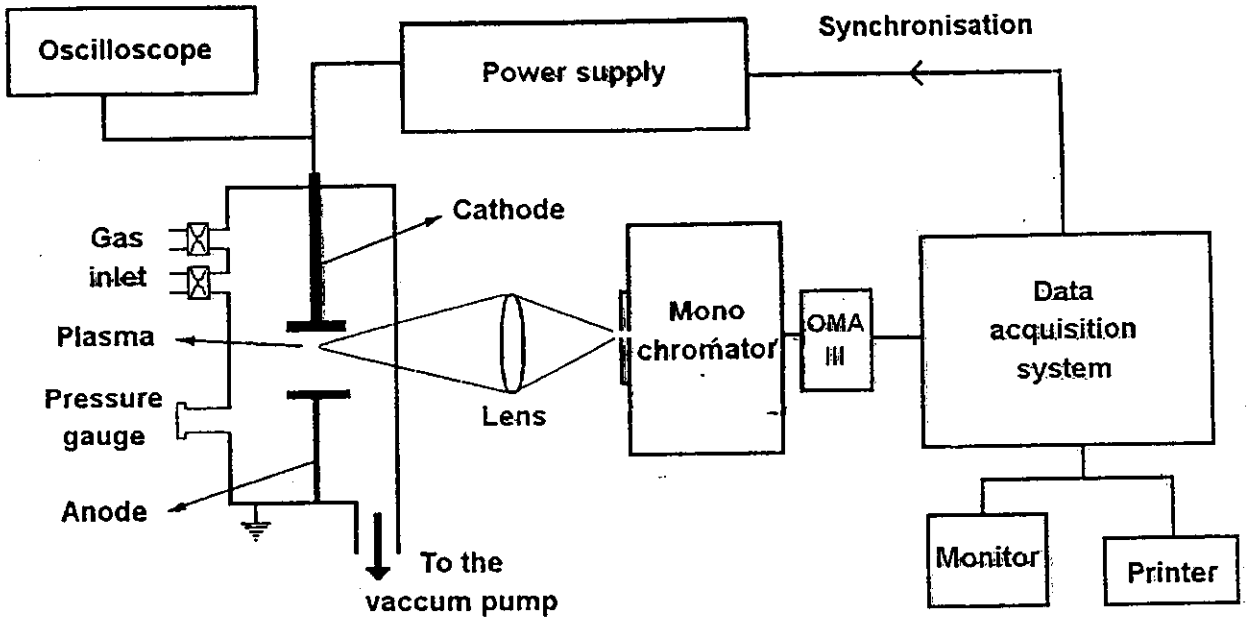

Fig. 10 Experimental set up of the real time optical spectroscopic study of the plasma activity during ion nitriding.

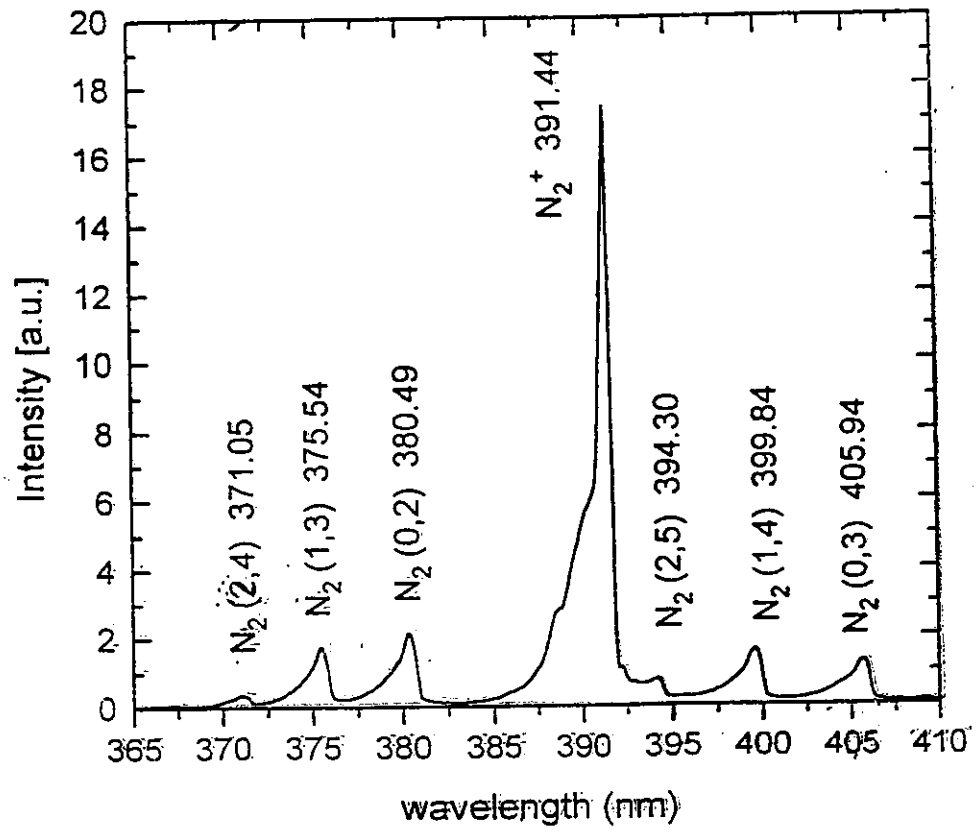

Fig. 11 Typical spectrum correspondig to a discharge glow discharge in 4 Torr in pure nitrogen

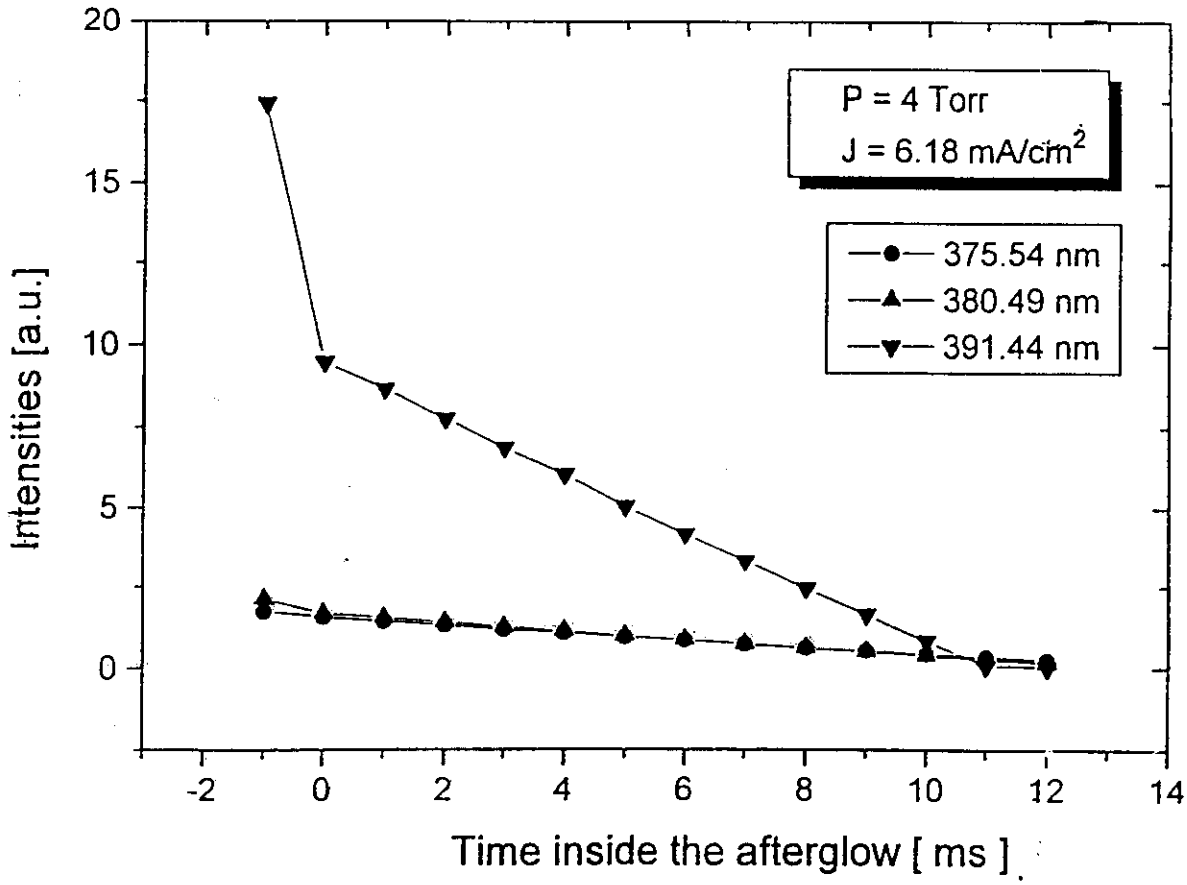

Fig. 12 Temporal variations of N_2^+ (391.44 nm) and N_2 (380.49 and 375.54 nm) band intensities.

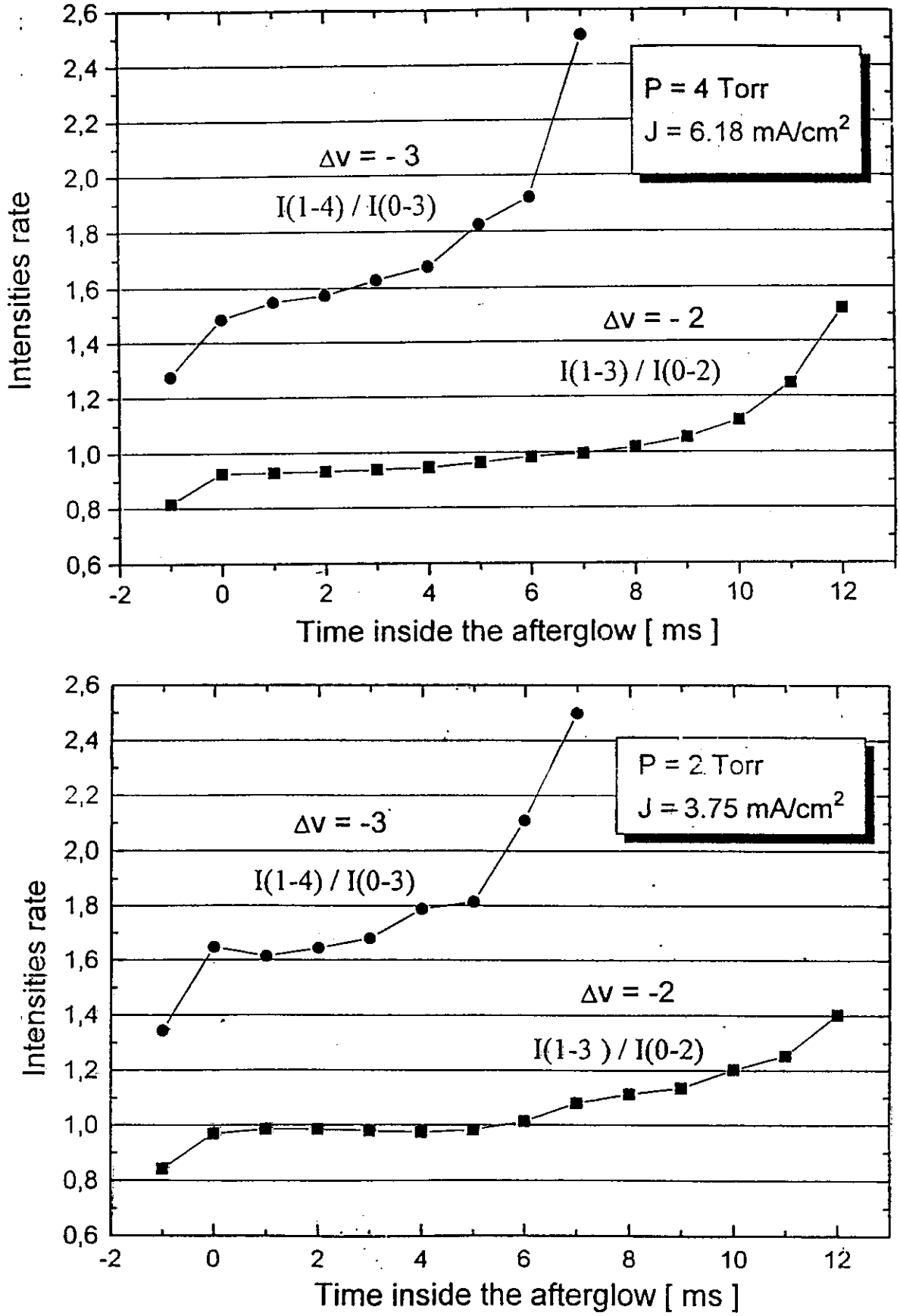

Fig. 13 The vibrational excitation between bands. The I(C,1-B,3)/I(C,0-B,2) and I(C,1-B,4)/I(C,0-B,3) intensity ratios during the discharge, as well as during the afterglow as a function of acquisition start time.

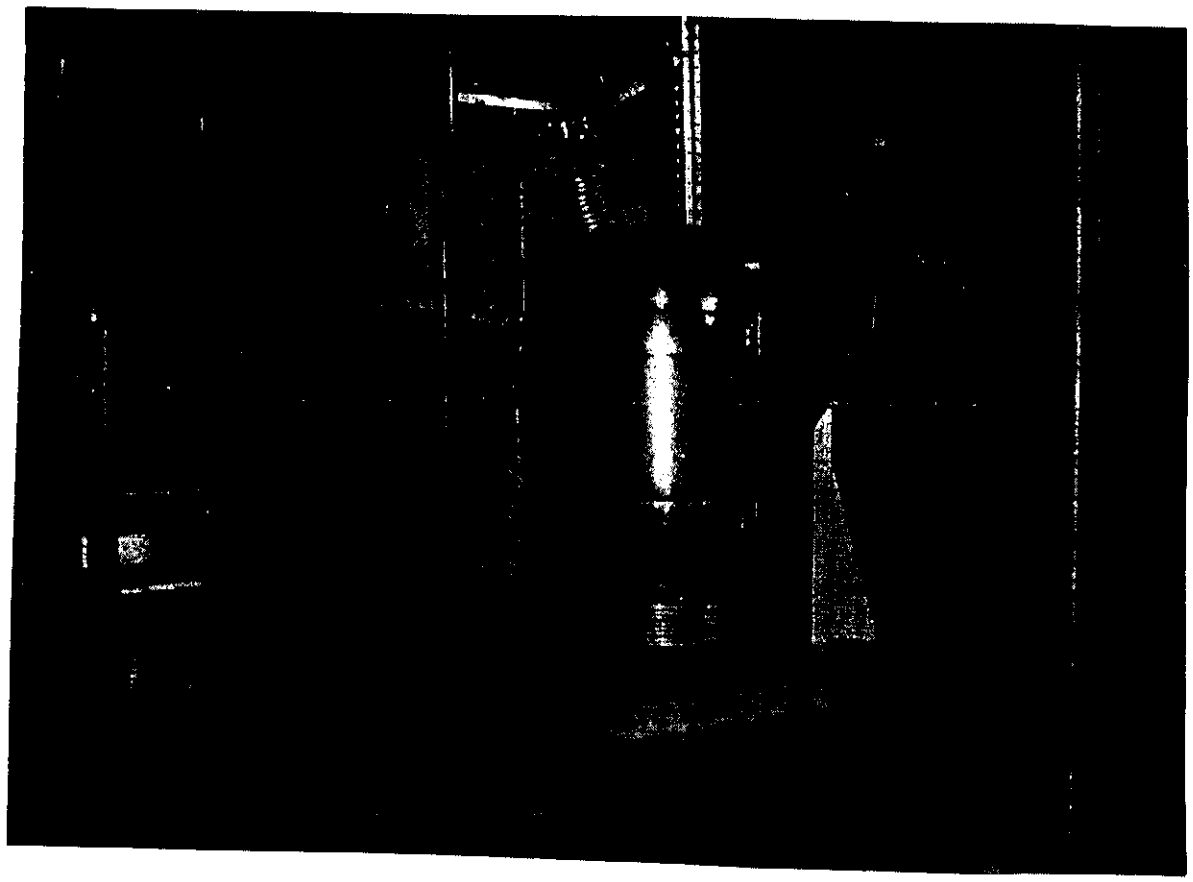

Fig. 14: Industrial reactor: reaction chamber.

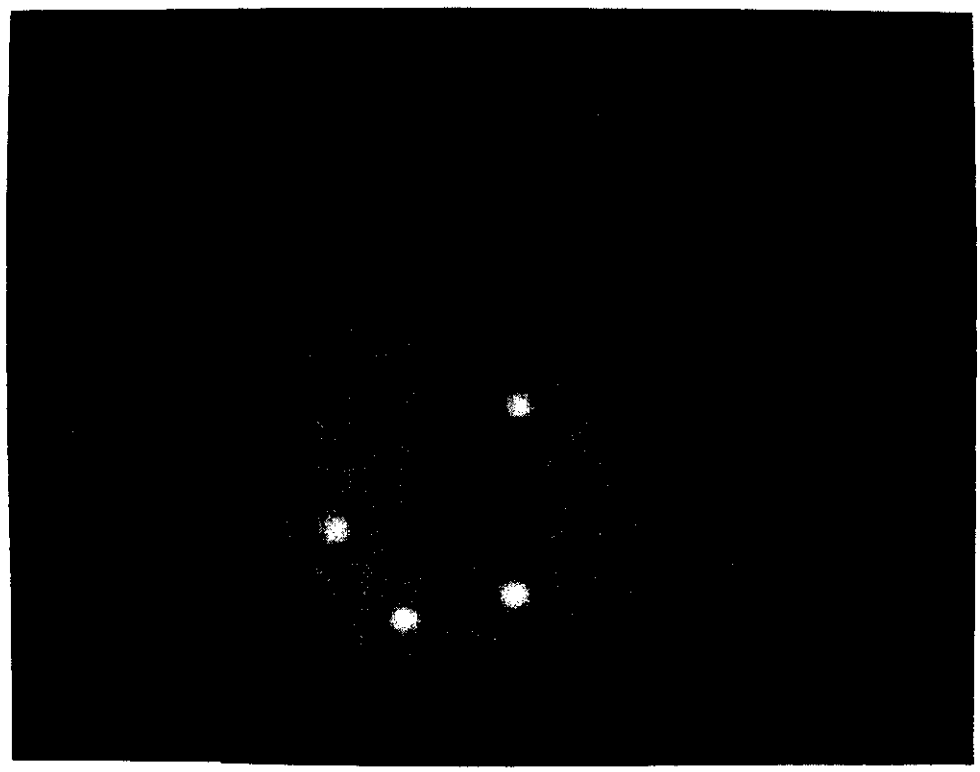

Fig. 15. Inside view of the chamber during ion nitring.